Austin Journal of Clinical Cardiology

Open Access

Austin Publishing Group

Review Article

Cardiac Progression of Biomechanical Risk Factor of Triple Vessel Disease and Biomedical Imaging on Right Coronary Arterial Hemodynamics

Sabrina Rashid[1]; M Ferdows[1*]; MA Xenos[2]; Mohammad Zahidur Rahman Mazumder[3]; KE Hoque[1]

[1]Research Group of Fluid Flow Modeling and Simulation, Department of Applied Mathematics, University of Dhaka, Bangladesh

[2]Department of Mathematics, Section of Applied and Computational Mathematics, University of Ioannina, Greece

[3]Anesthesia, Analgesia and Intensive care, Cumilla Medical College and Hospital, Bangladesh

***Corresponding author: Mohammad Ferdows**
Research Group of Fluid Flow Modeling and Simulation, Department of Applied Mathematics, University of Dhaka, Dhaka-1000, Bangladesh.
Email: ferdows@du.ac.bd

Received: January 09, 2024
Accepted: February 09, 2024
Published: February 16, 2024

Abstract

Cardiac Arterial Disease (CAD) is a common cardiac disorder characterized by the growth of atherosclerotic plaque in the arterial wall. Triple Vessel Disease (TVD) is the most acute type of CAD. The purpose of this study is to introduce a noninvasive method for cardiac hemodynamic parameter estimation with respect to Right Coronary Artery (RCA). In this work, we have constructed idealized RCA models with and without the side branch Posterior Descending Artery (PDA) which is a risk factor of TVD. A three-dimensional computational approach simulating steady and pulsatile blood flow in the constructed models is introduced. There are two computational domains, one consists of blood and other consists of the arterial muscle. The Arbitrary Lagrangian Eulerian (ALE) and the finite element methods have been used for the deformation of the arterial wall and its interaction with blood flow. Pulsatile arterial function induced a flow rate and pressure waveforms which are used at the inlet and outlet as the initial and boundary conditions for describing the flow. The biochemical interactions between blood and vascular tissue are neglected. The fluid-solid interaction results indicate that the severity of the stenosis increased the atherosclerosis progression. The average hemodynamic parameters such as velocity, pressure and wall stresses are substantially higher in arteries than in idealized arterial models, due to their complicated shape. As a result, it can be stated that the curvature and the side branches have a substantial impact on the hemodynamic analyses and their connection with atherosclerotic lesions. These findings can be utilized to envision the severity and the location of the coronary abnormalities and identify them in clinical practice.

Introduction

Coronary arteries are a network of vessels that runs through the middle of the heart. The delivery of oxygenated blood to the myocardium is their primary role. The left main coronary artery, which is divided into left anterior descending and circumflex branches, and the right main coronary artery are the principal arteries of the coronary circulation [1]. The Right Coronary (RCA) and the Left Major Coronary (LMCA) are the first two coronary arteries, both of which arise from the root of the aorta. Cardiac dominance is characterized by which coronary artery branch gives off the posterior descending artery and supplies the inferior wall. It is classified as left dominant, right dominant, or codominant [2]. The vessel most commonly originates from either the right coronary artery (right dominant), left circumflex artery (left dominant), or both (codominant). Right dominance serves as a risk factor for triple vessel disease. Triple vessel diseases are associated with higher rates of major adverse cardiac events and mortality than single and double vessel disease. While most Cardiac Artery Disease (CAD) may only impact one of the major coronary arteries, triple vessel disease impacts three major blood vessels [3]. The buildup of fatty materials, fibrous components, and calcium in the arteries is known as atherosclerosis. It is a progressive disease with symptoms that might take decades to appear. The early phases of the lesion are benign, but as the lesion progresses, it can narrow the vessel's lumen, resulting in a stenosis [4,5]. This stenosis obstructs blood flow and causes health problems. Coronary stenosis can be categorized based on where it occurs: proximal stenosis, at the beginning of the vessel; mid stenosis, in the middle of the vessel; and distal stenosis, at the end of the vessel. Almost 80-85% [6] of the human population have right dominant heart and they tend to have a high prevalence of triple vessel disease. The World Health Organization estimates that 17.9 million people

Citation: Rashid S, Ferdows M, Xenos MA, Mazumder MZR, Hoque KE. Cardiac Progression of Biomechanical Risk Factor of Triple Vessel Disease and Biomedical imaging on Right Coronary Arterial Hemodynamics. Austin J Clin Cardiolog. 2024; 10(1): 1108.

die each year from heart and blood vessel problems, accounting for nearly 31% of all fatalities worldwide [7]. These statistics are adequate to support further research in this area.

State of the art and Literature Review

Congestive heart failure with Triple Vascular Disease (TVD) has a greater death rate than acute myocardial infarction with single vessel disease or double vessel disease [8]. There are three main cardiovascular vessel such as Right Coronary Artery (RCA), left anterior descending artery and left circumflex artery. The term single-vessel Coronary Disease (CAD) is open to interpretation but is usually referred to as the presence of at least a 70% stenosis of major coronary arteries stated above or one of their respective major branches [9,10]. The double vessel disease has a reduction in cross-sectional area of at least 50% in two of the main coronary arteries. Finally, TVD is the cardiovascular disease which affects the three main arteries at once and causes the most acute myocardial infractions of all [11]. The role of the Right Dominance (RD) heart in the development of TVD has been intensively studied by many researches, analyzing the velocity, pressure and wall shear stress profiles. Peng et al. [12] suggested that the patients with RD tended to have a high prevalence of TVD and significant stenosis in the RCA. In conclusion, RD, rather than Left Dominant (LD) or Co Dominant (CD), was associated with triple-vessel coronary artery disease (CAD) in individuals. Left, right, or codominant heart dominance refers to which coronary artery branch stems from the posterior descending artery and provides the inferior wall [13]. This finding revealed that RD might be a risk factor for triple-vessel CAD, and that more effective interventions to avoid catastrophic cardiovascular events should be adopted in RD patients. Li Wang et al. [14] demonstrated that, 80-85% of the people have RD hearts and RD heart plays a significant role in TVD which causes acute myocardial infraction. So, a detailed study of the hemodynamics parameters of RCA of a RD heart should be performed.

O. Kafi et al. [15] have estimated that the risk of plaque rupture is higher in the event of a moving wall, whereas the risk of atheromatous plaque advancement is higher in the case of a stationary wall. N Pinho et al. [16] have analyzed that the physical properties of the right-ventricular branch (cross-sectional area) and the amplitude of wall shear stress in the intermediate and distal segments (PDA) were shown to have very strong correlations. So, the side branches are crucial to examine because they alter the outflow to the myocardium and have a significant impact on the capacity to detect abnormal patterns in hemodynamic parameters. Numerous *in vivo* and *in vitro* investigations have been undertaken over the last two decades to determine the association between the WSS and the change in luminal diameter over time using quantitative angiography. Gibson et al. [17] undertook three-year research to determine the rate of change in coronary artery diameter in individuals. They discovered a link between reduced shear stress and an accelerated rate of atherosclerosis development. The connection between WSS assessed *in vivo* and early atherosclerotic lesions in the abdominal aorta was investigated by Pedersen et al. [18]. They showed three scatter plots of relative intimal thickness as a function of mean WSS, maximum WSS, and oscillatory shear index, demonstrating that relative intimal thickness decreases linearly with mean and maximum WSS. Yang and Tang et al. [19] introduced a computational procedure based on a meshless generalized finite difference method and serial MRI data to simulate carotid atherosclerotic plaque progression. The numerically simulated plaque progression agreed well with the actual plaque geometry. L. Failer et al. [20] investigated the impact of Fluid-Structure Interaction (FSI) on the distribution of WSS and Fractional Flow Reserve (FFR). For comparison, they perform pure Navier–Stokes simulations on a pre-stressed geometry to ensure that the two configurations are well matched. The authors describe and analyze a series of numerical simulations that address essential hemodynamical parameters. Jun-Bean Park et al. [21] showed that by providing non-invasive measurements of WSS impacting coronary plaques, the cCTA-based Computational Fluid Dynamics (CFD) technique can enhance the detection of high-risk plaques and risk stratification for coronary artery disease patients. Using coronary CT angiography, they determined the distribution of pressure and shear-related forces acting on atherosclerotic plaques and their relationship to lesion characteristics. Liang Zhong et al. [22] demonstrated that creating patient-specific models takes time and necessitates patient-specific geometries, material qualities, and realistic boundary conditions. These are tremendous obstacles, in order to overcome these obstacles and obtain better outcomes, we constructed an idealized RCA geometry based on patient-specific models. Biyue Liu et al. [23] showed that the progression rate in a coronary artery was lower with a higher inlet flow rate and higher with a smaller value of the blood viscosity. Barbara M Johnston et al. [24] showed that when studying the wall shear stress distribution for transient blood flow in arteries, the use of a Newtonian blood model is a reasonably good approximation. So, in the present study we use the same assumption and the fluid-solid interaction interphase will be a good match for the approximation discussed in [24]. Haipeng Liu et al. [25] stated that different coronary plaques are consistent in the relationship between geometry parameters in different dimensions. Sarah Rinehart et al. [26] expressed that standardized, quantitative analysis of coronary CTA datasets is reproducible for the measurement of plaque geometrical and compositional parameters. This analysis can quantify differences between normal and abnormal segments in high-quality datasets. Haipeng Liu et al. [27] demonstrated in their study that, the methodological advancements are critical for more accurate CT-based coronary plaque evaluation in clinical applications. The three-dimensional geometry of coronary plaques may be used to infer more multidimensional geometric characteristics. Furthermore, in future investigations, machine learning and autonomous three-dimensional reconstruction may increase the efficiency of coronary plaque extraction. So, aim of present work is to analyze the coronary plaques by applying a software approach to get more accurate CT-based coronary plaque evaluation.

Maria Vittoria Caruso et al. [28] showed that, while the trans-stenotic pressure drop is linked to the minimum lumen area, stenosis geometry has a major influence on translational flow pattern and WSS. The goal of this work was to explore statistically the hemodynamic changes caused by stenosis geometry in a patient-specific RCA. The velocity pattern, the WSS distribution, the Oscillatory Shear Index (OSI), and the pressure field were all considered and evaluated in CFD simulations. The authors have used angiographically-guided model and computational fluid dynamics to reconstruct the local hemodynamics in a coronary artery. They considered three different plaque shapes in the main branch of RCA for analyzing the hemodynamic parameters. In the present study, we have modeled the main branch of RCA along with the most important side branch PDA which is the indicator of RD heart. Since, PDA is an important risk factor of TVD, we have analyzed the stenosed PDA and discussed its effect on the overall stenosed and healthy RCA.

The main goal of this study is to show the accuracy of the obtained RCA simulation with respect to patient-specific model. This will increase the efficiency of the visualization process of plaque progression. The additional aims of the present work are to study the geometrical adaptation of RCA with and without PDA and how is related to the Wall Stress (WS). To study the influences of flow parameters, such as flow velocity profile, pressure amplitude and WS profile on the plaque wall thickness increase by utilizing numerical simulations [28]. To examine the local flows in curved RCA with increasing stenosis, numerical simulations are performed under a range of 2-cardiac cycles. The initial computational domain is simplified and it is based on a three-dimensional patient-specific RCA model reconstructed from a series of angiograms.

Cardiac Model of RCA

Construction of the Three-Dimensional Geometric Model

Most of the stenosis occur at the artery's bending points. To characterize these aspects, we created an idealized model based on a patient-specific computed tomography coronary artery angiography models with stenosis at various locations and a side branch PDA. In this study, computer-aided design program "Free CAD" is used to create the three-dimensional idealized models, which are then loaded to "COMSOL Multiphysics" software for grid creation and simulation. Free CAD software [29] is used to create the three-dimensional idealized models and we have constructed two healthy models. The first model consists of the main body of RCA which is divided into proximal, mid and distal segment. The length of the proximal part is 3.26±0.79 mm, the mid part is 3.45±0.74 mm and the distal part is 3.55±0.77 mm [30]. We have reconstructed the geometry with lengths 3.2 mm, 3.4 mm and 3.5 mm for the proximal, mid and the distal parts, respectively. The branch from PAD artery has a length of 12 mm [31]. The structure and dimensions of the models are anatomically based on a typical RCA. We have taken four diseased models. The "1-stenosis" model consists of one stenosis in the proximal region, the "2-stenosis" model consists of a stenosis in the mid region along with the 1st discussed stenosis, the "3-stenosis" model consists of a stenosis in the distal region along with the 1st and 2nd discussed stenosis. Finally, another multiple stenosis model is reconstructed consisting of a stenosis in the PDA branch.

To curve the models, we use B-splines which are easy to represent the bending nature of the RCA and the side branches. For building the arterial wall we again use B-splines with the same center but different radius. Taking the difference of radii, we build the arterial wall for the blood flow. Using Boolean functions, we can get accurate shapes of the three-dimensional idealized models [32]. In the diseased model the stenoses are generated using the software. The first computational idealized model contains one inlet and one outlet and the other one contains one inlet and 3 outlets that are represented by outlet *i*, *i* = 1, 2, 3, 4. The radius of inlet is 1.2 mm and the radius of outlet is 1.5 mm. Again, the radius of side branch outlets is 1.1 mm. RCA cardiac model with and without PDA has been discussed in brief as follows:

RCA Cardiac geometry modeling:

a. Main body consisting of proximal, mid and distal segments (Figure 1)

b. body with side branch PDA (Figure 2)

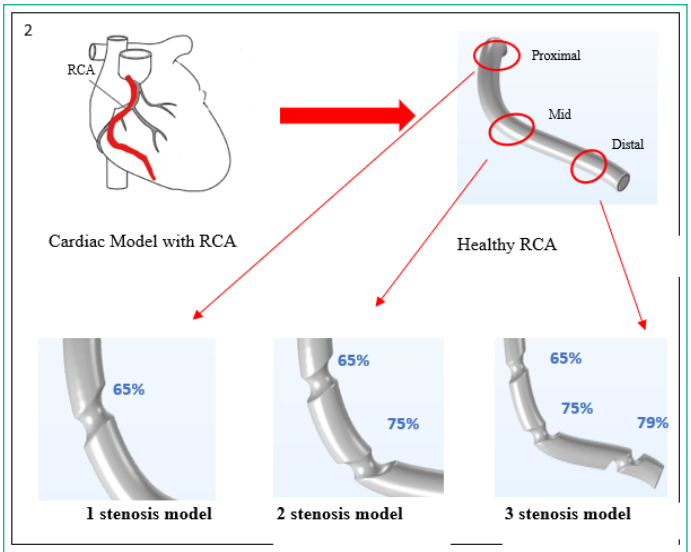

Figure 1: RCA (without PDA) with multiple stenosis.

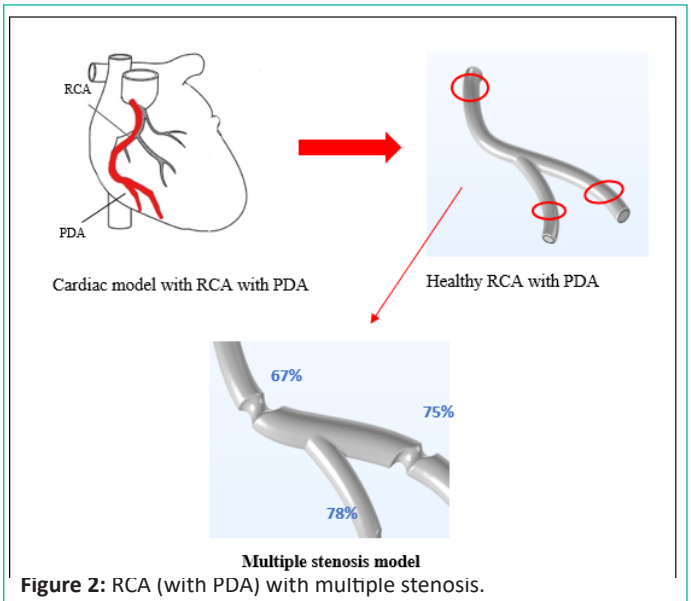

Figure 2: RCA (with PDA) with multiple stenosis.

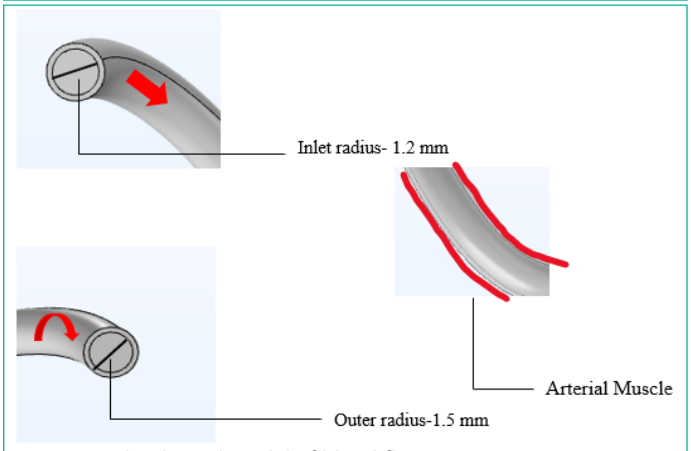

Figure 3: Rheological model of blood flow.

The stenosis severity is calculated by the following formula

$$SV\% = \left(1 - \frac{D_s}{D_a}\right) \times 100\%$$

Here, SV= Stenosis volume, D_s = Diameter of the stenosis and D_a = Diameter of the artery.

Mathematical Modeling of Cardiac Flow

Blood may be represented as an incompressible fluid with a density of 1,060 kg/m3 and Newtonian behavior. For shear rates greater than 100 s-1, this last assumption is widely accepted.

However, because there are times throughout the cardiac cycle when the shear rate is less than the predefined threshold [33,34] non-Newtonian effects may become significant. As a result, we used the Carreau model [35] to analyze the Newtonian and non-Newtonian behaviors in the context of a healthy RCA. Furthermore, blood flow was hypothesized as laminar and three-dimensional Navier-Stokes equations were used,

$$\rho\left(\frac{\partial u}{\partial t}\right) + \rho(\boldsymbol{u}\cdot\nabla)\boldsymbol{u} = -\nabla p + \nabla\cdot\{\mu[\nabla\boldsymbol{u} + (\nabla\boldsymbol{u})^T]\}$$

$$\nabla\cdot\boldsymbol{u} = 0,$$

where, ρ is the fluid density, $\boldsymbol{u}$ and p are the fluid velocity and pressure.

We have used the FSI problem. Let Ω^f and Ω^s be the domains occupied by the fluid and the solid, respectively, in their reference configuration. We denote by $\Gamma = \partial\Omega^f \cap \partial\Omega^s$ the fluid–structure interface on the reference geometries. The Arbitrary Lagrangian-Eulerian (ALE) approach [36,37] can extract the fluid domain $\Omega^f(t)$ from Ω^f at any time, $t \geq 0$.

Using the ALE formulation, the volumetric finite element grid in $\Omega^f(t)$ may be reconstructed arbitrarily from the one on the domain borders, $\partial\Omega^f$. This reconstruction is performed directly on the reference configuration for the sake of calculation by applying an extension of the structure displacement d_s at the fluid–structure interface to the interior of the fluid domain,

$$\begin{matrix} \boldsymbol{d}_f = \boldsymbol{d}_s \\ \boldsymbol{\sigma}_f\cdot\boldsymbol{n}_f = \boldsymbol{\sigma}_s\cdot\boldsymbol{n}_s \ \ on\,\Gamma \\ \boldsymbol{u}_f = \boldsymbol{u}_s \end{matrix} \qquad (0.4)$$

Where $\boldsymbol{n}_f$ is the outward unit normal to the reference fluid domain border and $\boldsymbol{n}_s$, is the inward unit normal to the reference fluid domain boundary. Because the structural displacement d_s vary over time, the periodic outgrowth [38] may be used to determine the fluid domain's precise configuration. The fluid dynamics are regulated by the incompressible Navier–Stokes equations expressed in the ALE framework [39]. Equation (2.1) can be written in the ALE formulation as follows,

$$\rho_f\left(\frac{\partial\boldsymbol{u}}{\partial t}|_\lambda + (\boldsymbol{u}-\boldsymbol{w})\cdot\nabla\,u\right) - \nabla\cdot\boldsymbol{\sigma}_f(\boldsymbol{u},p) = 0 \qquad (0.5)$$

Where, $\boldsymbol{w}$ is fluid mesh velocity, $\frac{\partial d_f}{\partial t}|_x$.

The conservation of momentum for the solid structure in Lagrangian form becomes,

$$\rho_s\frac{\partial^2 d_s}{\partial t^2} - \nabla\cdot(WS) = 0 \qquad (0.6)$$

Where, ρ_s is the density of the solid structure, d_s is the displacement of the solid, and *WS* is the solid stress tensor on the arterial wall. The coupling between the geometry and fluid is represented by,

$$\boldsymbol{d}_f = \boldsymbol{d}_s \qquad (0.7)$$

$$\frac{\partial\boldsymbol{d}_s}{\partial t} = \boldsymbol{u}\cdot A_t \qquad (0.8)$$

Equation (2.7) is an interface condition where it describes the displacement at the interface and how it is transferred to the fluid domain, in contrast to the no-slip condition. Equation (2.8) is for introducing the fluid loading on the arterial geometry. Because of the moving fluid domain, the convective term in the fluid momentum equation, and the coupling of the structural material model, the resultant system of equations defining the FSI problem is substantially nonlinear.

Blood Rheology

The science of coupling the material deformation and flow is known as blood rheology. It describes the interrelationship between force, deformation, and flow using theoretical ideas of kinematics, conservation laws, and structural formulations [40,41]. The macroscopic behavior of blood as established by rheometric studies, its microscopic qualities *in vitro* and *in vivo*, and investigations of interactions between blood biological components and the endothelial cells that line blood arteries are all part of this field.

With increasing flow velocity and shear strain rate, blood flows smoothly and its viscosity decreases toward a constant, which has been commonly used as the viscosity of blood in a Newtonian model [42]. Many factors impact the complicated rheology of blood, including plasma viscosity, shear rate, hematocrit, erythrocyte aggregation levels, and deformability. The vascular wall deformability is taken to be elastic while the flowing blood contained in it is treated to be Newtonian [43]. While plasma behaves almost Newtonian, entire blood has distinct non-Newtonian features, especially at low shear rates. The tendency of erythrocytes to develop a three-dimensional microstructure at low shear rates, their deformability, and the radius of the vessel all contribute to blood's non-Newtonian behavior [44].

Since, the radius of the RCA allows the blood to flow smoothly and the fluid-structure interaction phase only allows the blood to exert force on the arterial wall, we can approximate the blood as a Newtonian fluid. The error caused from this assumption can be ignored. The pulsatile inlet and outlet flow conditions are imposed since the complicated vessel shape of the entire vascular system can neither be measured nor completely materialized [45,46]. So, the Newtonian modeling approach can be used for the computational hemodynamic simulation. The cardiac cycle is a pulsatile, closed-loop mechanism in which the heart pumps blood throughout the systemic circulation in a rhythmic (periodic) pattern. We assume that the cardiac cycle begins with systolic phase and that the systole time is 2/5th of the cardiac cycle period. Arterial Compliance, Vascular Rigidity, and Inertia are each represented by a capacitor, resistor, and inductor simplified model [47]. The basic Windkessel method estimates the systolic and diastolic stages of the heart cycle to produce a consistent exponential pressure curve.

It was established that the chosen inlet velocity condition had a substantial impact solely on the flow zone near the aorta's inlet. Similarly, the outlet conditions chosen to have a considerable impact on the flow in the outlets' region [48]. Several researchers found that adopting a well-tuned three-element Windkessel model [49] at all model outlets resulted in the best overall performance, not only in terms of agreement with *in vivo* peak flow, but also in terms of functional pressure waveforms and values. So, we choose the inlet and outlet velocity and pressure waveform as a three-element Windkessel model. The characteristic impedance is described by an oscillating phenomenon that can be explained in terms of oscillatory dynamics which is similar to cardiac flow patterns [50,51].

The radius, shown in Figure 3, allows to follow the Newtonian rheological approach and the arterial wall as a linear elas-

tic. The blood enters the inlet, flows smoothly throughout the inner vessel which interacts with the arterial muscle and flows out of the domain at the outlet.

Computational Approach

Domain Discretization

The initial step in numerically solving the continuity and Navier-Stokes equations is to create a computational mesh. It is necessary to design a high-quality grid to obtain accurate results [52]. Over curving edges and volumes, finite element grid formation provides a clear and complete approach. A nonstructural mesh of tetrahedral components was used to create the grid of the structures and the fluid domain.

For all RCA models, the isotropic mesh was established in the three-dimensional computational domains with parameters such as global maximum edge size (1.55 mm for fine mesh) and advanced options. We added boundary layers to the computational domain wall, a 0.543 mm edge element, and a layer decreasing ratio of 0.3 in the advanced settings. The total number of meshes in the first RCA model was 3,859,500 and in the second model was 9,678,100 approximately. The enlarged views of the essential mesh portions such as inlet, outlet, bending segment and the stenosis of the RCA model are shown in Figure 4:4. The mesh convergence test results of the RCA model are calculated.

Grid Independency Study

Grid independency test determines how many elements are required in a model to ensure that the mesh size has no impact on the analyses' outcomes. Extra mesh refinement has little effect on the findings after convergence has been reached to the desired accuracy. The model and its output are now independent of the mesh. Numerical discretization approaches, such as the Finite Volume Method (FVM) converges to a solution only after a mesh independency study. So, mesh independence is important and extra refinement isn't essential after obtaining the required accuracy [53]. For various mesh densities, a grid independence test for velocity magnitude was performed. The mesh sizes ranged from coarse (number of elements: 92,210) to fine (number of elements: 1,780,357). The coarse grid generated 8.8% difference when compared to the smaller grid in the grid test (extremely fine grid).

The finer meshing results in improved components, promote model accuracy and raise the chances of obtaining a viable solution. The interface and outer area of the adaptive tetrahedral cells are imported into the Finite Element Method (FEM) program. Minor mesh changes are made to remove unnecessary elements and nodes, as well as to improve element density main stem of the coronary artery bending and stenosis. The other parameter settings of the meshing are the growth rate of the boundary layer, defined as 1.5, the curvature factor 0.7, and the resolution in narrow regions defined as 0.5. For grid independence test, we have taken extremely coarse, normal and fine mesh and the respective parameters stated in the Table.

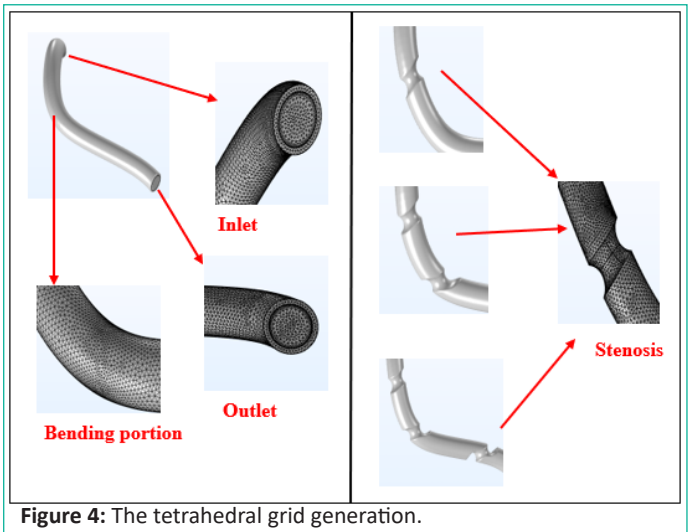

Figure 4: The tetrahedral grid generation.

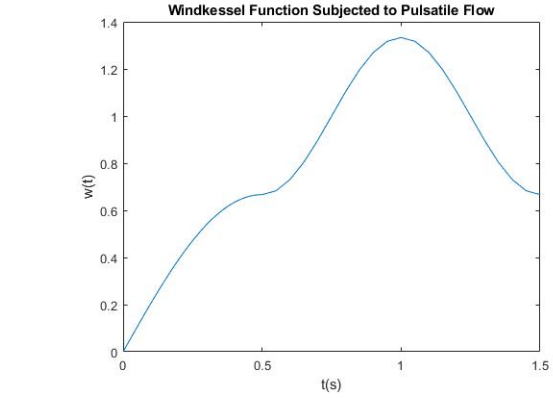

Figure 5: Windkessel function subjected to pulsatile flow.

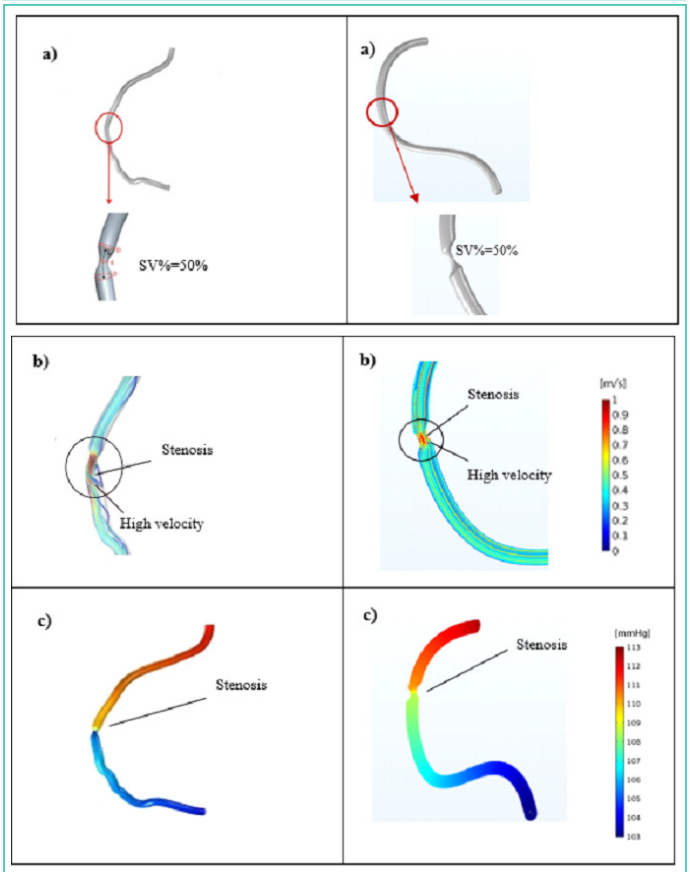

Figure 6: Validation of the approach and comparison of (a) the geometry, (b) streamlines of the flow field colored by the velocity magnitude and (c) pressure field.

Utilizing these tabular values in the finite elements solver, the grid independency for velocity amplitude shows the accuracy of the numerical results in Table. Since the normal and fine meshes provide almost similar values for the maximum velocity magnitude in the computational domain, we can conclude that the result will not be varied for finer and extremely fine meshes. So, the finite element approach introduced to solve the cardiac model is convergent. Therefore, for the present study, a grid size of 70,200 has been used to perform all the simulations.

Table 1: Parameters for grid independence test generation.

Element size	Coarse	Normal	Fine
Maximum size	0.434	0.279	0.062
Minimum size	1.6	1.5	1.4
Curvature factor	0.7	0.6	0.4
Resolution	0.4	0.5	0.7

Table 2: Grid independency test values for maximum velocity magnitude.

Mesh	Element Number	Max. Velocity magnitude [m/s]
Coarse	92,210	0.38
Normal	105,000	0.42
Fine	1,780,357	0.425

Table 3: Material properties of the arterial model.

Domain 1 (Blood)	Domain 2 (Arterial muscle)
Density $(\rho) - 1060\ kg/m^3$	Density $(\rho) - 960\ kg/m^3$
Dynamic viscosity $(\mu) - 0.005\ Pa.s$	Linear elastic properties $= \begin{cases} \text{Lame parameter } \mu = 6.20 \times 10^6 \\ \text{Lame parameter } \lambda = 20 \times \mu \end{cases}$

Boundary Conditions

In idealized RCA models, accurate Boundary Conditions (BCs) are critical for producing high-quality physiological heart flow simulations. There are various BCs such as analytic, implicit, explicit, Windkeseel BCs. These BCs can be applied on lumped parameter models, or low-dimensional models on the basis of criteria. Windkessel BCs applied on lumped parameter model gave an almost accurate simulation of idealized RCA hemodynamics [54].

In the RCA models, we used Windkessel BCs for pulsatile flow in conjunction with lumped restrictions for a hyper elastic material [55]. The heart pressure and flow are periodic in time, with period T. The single heart beat takes up approximately 0.8 second. We have simulated two cardiac cycles, and approximate time is 1.5 seconds. We can use the following function as the arterial input function [56] from which we can produce inlet velocity profile and outlet pressure waveforms.

$$w(t) = \begin{cases} (1-\alpha) * sin(\pi t), & 0 < t < 0.5, \\ 1 - \alpha * cos\left(2\pi(t-0.5)\right), & 0.5 < t < 1.5. \end{cases} \quad (0.9)$$

Equation (3.1) is a trigonometric function, α, is the Windkessel parameter indicating the relative pressure amplitude. During a cardiac cycle, pressure changes between a minimum and a maximum value, which is determined by a relative pressure amplitude α, which has a value of 3. The first piece of function between 0 and 0.50 s has used to produce inlet velocity profile at initial state. The second piece of function makes the pressure vary between its minimal and maximal value during an approximately one second cardiac cycle. The pressure and velocity magnitudes for the idealized RCA model are determined by the computational findings. The arterial input function is shown in Figure 5. To describe the pulsatile flow, we used the input velocity profile illustrated in Figure 5. In the arterial region, the explicit inlet velocity waveform induces pulsatile activity [57]. We've specified an outlet pressure waveform, continuous over the outlet face.

The intramyocardial pressure is included in the Windkessel model (outflow waveform), which keeps the coronary circulation out of phase with the systemic circulation [58]. The generated models reflected accurately the coronary physiological flow characteristics during the entire cardiac cycle.

The velocity and pressure profiles are employed as BCs in the finite element approach for solving the governing equations under consideration.

Cardiac Hemodynamic Simulations

We perform pulsatile blood-flow simulations by numerically solving the system (2.4) - (2.7). The simulation setup that includes material parameters has been inspired by the benchmark paper [36,59]. But we have changed some of the values to keep pace with the specifications of this study. There are two types of material included for the two domains, fluid and solid. Firstly, the blood properties are employed on the fluid domain and the lumped parameter arterial properties are employed on the solid mechanics domain.

A finite element-based software tool was used in this computational study. Time-dependent simulations were performed in all situations, with a time step of dt = 0.01 s. Furthermore, for both the velocity components and the pressure field, the elements employed in the finite element formulation were linear (P1+P1).

Finally, we use the provided finite element framework to examine several hemodynamic parameters important to clinical outcomes. More precisely, we concentrate the attention on the relationship between these characteristics and the elasticity of the vessel walls, as well as their importance to material properties. Fluid-structure interactions (fluid loading on geometry) require significantly more work than only solving the Navier–Stokes equations, which should be justified by equivalent consequences. Three particular parameters' behavior is explored. The WSS is important in a variety of applications. It's utilized to predict the progression of atherosclerotic plaques [60].

However, going a step further, we investigate the impact of various complexity, such as Navier–Stokes and FSI, on the wall stress (WS) distribution of the arterial wall, in both geometries. Furthermore, we analyze the velocity profile with respect to arc length. This observation can provide approximate plaque locations. Finally, the magnitude of the pressure fluctuations throughout two cardiac cycles is discussed. After a stenotic area in a blood artery, the amplitude generally lowers substantially in clinical assessment.

We will show that this impact can only be represented by using the coupled model containing elastic vessel walls by comparing coupled fluid-structure interactions with the clinical data. The results of the simulations, obtained for realistic system parameters, are in good qualitative agreement with these observations.

Approximation of complex systems of fluid and solid equations remains a significant difficulty, particularly in three-dimensional applications. There are just a few fast solutions for the nonlinear situation [61]. The proposed method relies on a multigrid solution that looks to be superior in three-dimensions. We provide the solution strategy in [62], which is based on a Jacobian partitioning based on two steps:

1. The resulting nonlinear solver is an approximated Newton method that accurately solves the original problem since the residual is exact. Failer et.al. [63] have found that such an approximated Newton solver is even more efficient, despite slightly increased iteration counts. This is due to the very costly evaluation of the full Jacobian that is not required in our approach.

2. We exploit the discretization of the equation $d_t u_s = v_s$. Precisely, if we consider the Crank–Nicolson scheme, this transformation allows to completely remove the new solid deformation u_n^s from the discretized momentum equation.

Result and Discussion

Validation of the Models

To validate the performed simulations and the obtained solutions, the Windkessel's model is used as the boundary condition in simulating blood flow rate and pressure during the cardiac cycle.

We have constructed a model with a parabolic stenosis as observed in the most severe cases. The stenosis is 50% as per the literature data. The simulation was performed under the same boundary conditions and data configuration. The streamlines of the velocity magnitude are reported to examine the flow pattern. They are evaluated at the time instant, t = 0.575 s, in which the maximum flow rate occurs. The velocity streamlines are in a good agreement with this profile.

The minimal lumen area is the major determinant of transstenotic pressure drop, which is evaluated for establishing the clinical importance of stenosis. The calculated pressure field is also in a good agreement with [59]. Calculated velocity fields and pressure amplitude for the proximal position of the RCA (without PDA) is presented below and compared with previously published data in Figure 6. The SV% is calculated exactly [59]. The calculated velocity varies between 0 to 1 m/s and pressure varies between 103 to 113 mmHg which are in good agreement with previously published data.

Hemodynamic Flow - Presentation of Velocity, Pressure and WSS

For performing numerical computation of the desired quantities of major physiological significance, the following parameters have been visualized and presented in detail.

The velocity, pressure, and WSS values are estimated for various degrees of stenosis models at definite times and positions of the RCA curve. The pulsatile waveforms introduced hemodynamic properties in the numerical simulation. The variation of the degree of stenosis shows the variation in the hemodynamic parameters. The numerical results present in this section are obtained during the systolic peak, that is, when the time is t = 0.4 s.

The constricted section of the arterial lumen is referred to as the stenotic zone. Increased velocity in the stenotic zone is the single most important doppler result (in ultrasound measurements) for evaluating the severity of artery stenosis. Because the same volume of blood must flow through the constricted lumen as through the wider, normal lumen, flow velocity is enhanced in the stenosis. The degree of luminal constriction is directly related to the rise in stenotic zone velocity [64]. To evaluate the severity of arterial stenoses, three stenotic zone velocity measures are usually utilized. First, peak systolic velocity (also known as peak systole), which is the highest systolic velocity within the stenosis, secondly, end-diastolic velocity (also known as end diastole), which is the highest end-diastolic velocity; and lastly the systolic velocity ratio, which compares peak systole within the stenosis with peak systole proximal to the stenosis (in a normal portion of the vessel) [65,66].

We observe the velocity fields of the scenario 1 models. The healthy model (Figure 7(a)) demonstrates a uniform velocity profile and the stenosis models shows a variation. When stenotic lesions are characterized by their location, the velocity of the stenotic lesions is much higher in the more proximal site. The healthy RCA shows velocity variation between 0.05 to 0.35 m/s whereas the stenotic models vary between 1 to 10 m/s. At proximal position (Figure 7(b)), the stenosis volume is 65% and the velocity varies mostly in this position even though the stenosis is less severe than the mid and distal position. In 2 stenosis model (Figure 7(c)), the mid position consists of 75% stenosis and in 3 stenosis model (Figure 7(d)), the distal position consists of 79% stenosis. These two models are more severe but due to the position their velocity is less than the proximal one.

Scenario 1: Velocity Fields

In Figure 8, the velocity of branched healthy and diseased RCA has been visualized. The velocity of the healthy branched RCA is uniformly distributed between 0 to 0.5 m/s whereas the velocity of the stenosed branched RCA is varying between 0 to 2.5 m/s. This increment is indicating the severity in the velocity field which is much less than the proximal stenosis because the PDA is at a distal location.

A stenotic arterial lesion that lowers the artery's cross-sectional area produces a loss of kinetic energy, and pressure reduction [67]. As expected, the pressure drops to a greater extent at 3 stenosis model (Figure 9(d)) than at the 1 stenosis model (Figure 9(b)). Thus, the blood encounters relatively lesser resistance in 3 stenosis model than 1 stenosis model. It is observed that the pressure drops higher for the 79% stenosis at the 3-stenosis model as compared to the 65% stenosis at the 3-stenosis model. These findings reveal a strong relationship between intra-arterial and measures of pressure drops induced by arterial stenoses in scenario 2.

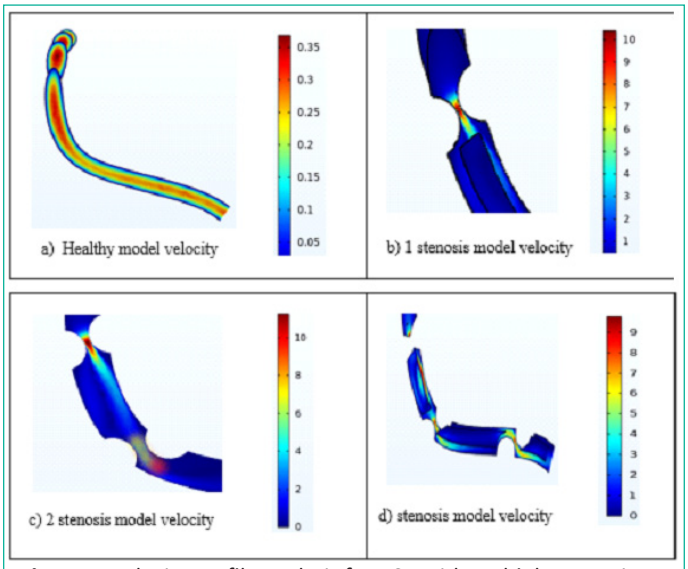

Figure 7: Velocity profile analysis for RCA with multiple stenosis (without PDA).

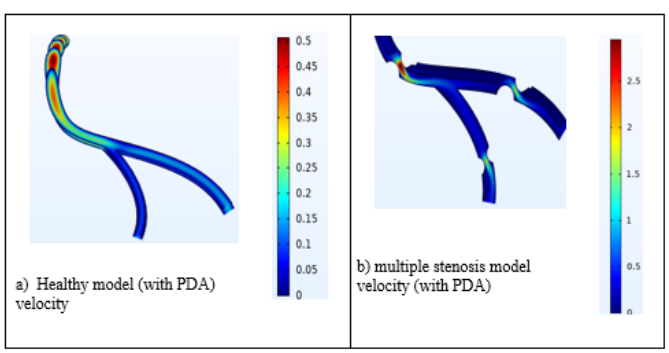

Figure 8: Velocity profile analysis for RCA with multiple stenosis (with PDA).

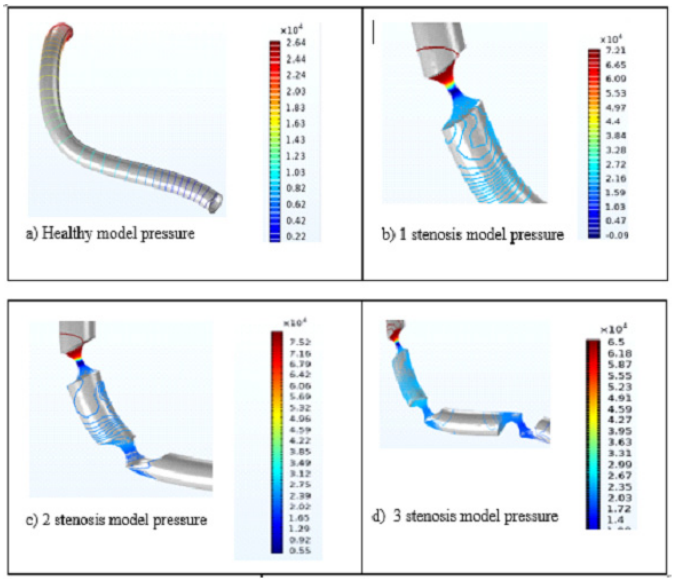

Figure 9: Pressure profile analysis for RCA with multiple stenosis (without PDA).

Scenario 2 briefly elaborates the pressure distribution and comparison between the healthy and diseased state. The healthy model demonstrates a uniform pressure profile distributed between 0.22×10^4 to 2.64×10^4 Pa and the stenosis models shows a variation. The 1 stenosis model consisting of the stenosis in the proximal location shows less pressure drop than the 2 stenosis and 3 stenosis model consisting of the stenosis in the mid and distal location. At mid location, there is 75% stenosis, and the respective pressure drop is between 0.55×10^4 to 7.52×10^4 Pa which is lesser than the distal location which consists of 79% stenosis. The respective pressure drop for the distal location is 1.4×10^4 to 6.5×10^4 Pa.

In Figure 10, the branched RCA have more severe stenosis in the PDA branch (79%), it shows larger pressure drop than the previously discussed stenosed model. It varies between 2.14×10^4 to 2.71×10^4 Pa. Hence, we can conclude that, unlike the velocity, the pressure drop does not depend on the location but it depends on the severity of the stenosis area percentage and the shape of the stenosis. This finding can help the physician to determine the stenosis severity.

Scenario 2: Pressure Variations

Over the years, several hemodynamic descriptors based on WSS have been developed to investigate hemodynamic flow instabilities as biomarkers [68]. These findings raised the point that the WSS distribution and magnitude are greatly influenced by the size, symmetry, and position of the atherosclerotic plaque. However, the Wall Stress (WS) effects are difficult to quantify because require advanced FSI approaches. So, in this study and effort is made to evaluate the WS along the stenosis of the pathological artery wall as well as neighboring walls. In stenosis, the largest magnitude of WS is recorded in the proximal location.

Furthermore, the stenosed wall and high curvature sections have a high WS.

In scenario 3, the WS distributions along the RCA with and without PDA at the peak systole are shown in Figure 11:11 and Figure 12:12, respectively. The areas with maximum WS can be observed along the proximal location. The healthy RCA has a uniform distribution of WS other than the curvature part. In the 1 stenosis model (Figure 11:11(b)), the maximum WS is 1.4×10^6 Pa which is the highest among 2 stenosis model (Figure 11:11(c)) and 3 stenosis model (Figure 11:11(d)). Even though the severity of stenosis in distal location (79%) is higher than that of the proximal location (65%), the value WS is higher in the proximal location.

In branched RCA, the value of WS at peak systole phase is 8×10^4 Pa (Figure12:12) which is less than the value of WS of 1 stenosis model. The reason behind this is, the stenosis at PDA branch is at a distal location. So, even though the severity of stenosis is higher (79%) than the 1 stenosis model, the value of WS amplitude at systole peak is lower than 1 stenosis model.

The flow environment of a diseased coronary demonstrates that the WS is also dependent on the curvature of the geometry and the location of the stenosis. The WS is affected locally along the stenosed artery wall as well as neighboring walls due to the stenosis. The highest WS value is seen in the stenosis of proximal location, indicating a significant risk of plaque rupture. High forces occurring on or within the arterial wall might cause the arterial plaque to break apart.

The degree and distribution of stenosis in the periphery are critical geometric parameters that influence the probability of fracture. These computational findings could help physicians and will allow them to link hemodynamics to the genesis and progression of atherosclerosis in the coronary arteries.

Scenario 3: Arterial Wall Stress (WS) Fields

In the next section, we take under consideration the cross-sectional area of the stenosis location and compare with the cross section of a healthy RCA at that exact same location.

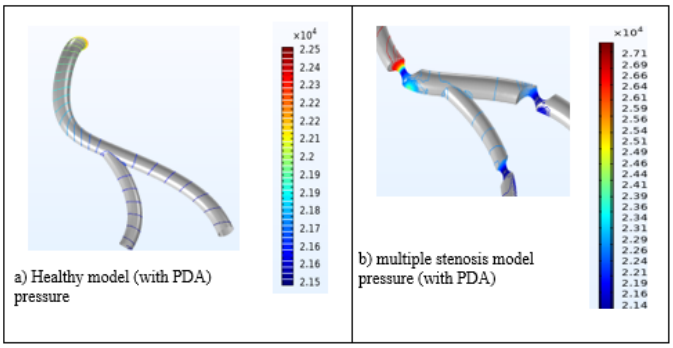

Figure 10: Pressure profile analysis for RCA with multiple stenosis (with PDA).

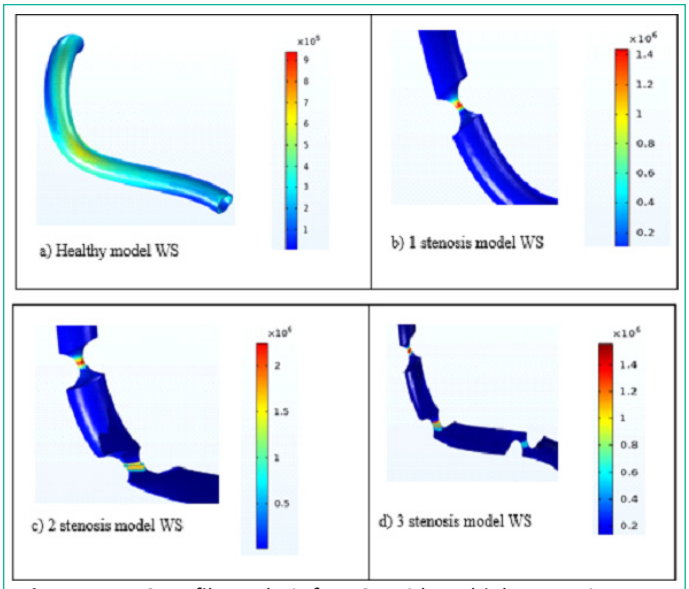

Figure 11: WS profile analysis for RCA with multiple stenosis (without PDA).

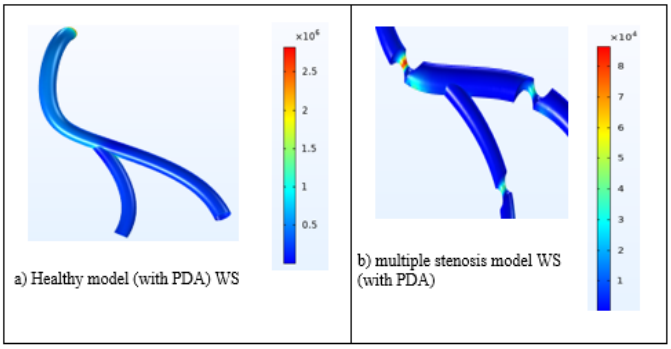

Figure 12: WS profile analysis for RCA with multiple stenosis (with PDA).

Hemodynamic Flow (Velocity and Pressure) for Cross-Sectional Areas

The RCA contains significant curvature and branches, leading to disturbed blood flow, and as an extent to stenosis and atherosclerosis [3,69]. Myocardial flow perfusion is reduced, resulting in myocardial ischemia and infarction. To better understand the processes underlying these occurrences induced by high curvatures and branching of coronary arteries, we conducted a detailed hemodynamic study using modeled coronary arteries with geometrical characteristics that reflect curvatures and stenosis. To begin, we calculated the hemodynamic parameters such as velocity and pressure, as well as their relationship with the geometrical parameters of curvature and stenosis, in idealized coronary arteries with approximated genuine artery geometry indicative of their curvature and stenosis. The arteries can be perceived as a mix of different bent segments with stenoses in random places. For better visualization we take the cross-sectional area of the portion where the stenosis occurs and to compare it with the healthy state, we took the cross-sectional area in the same location of the healthy artery.

In Figure 13:13, the encapsulations show higher velocity and pressure proximal to the stenosis. The first row shows the contour plots of the velocity profile for a healthy and stenosed artery at the proximal location with same area. Because there is no-slip, higher velocity is observed in the core portion of the artery, whereas lower velocity is found at the wall. In the right side, the velocity contours of stenosed artery are shown. They are parallel at lowest input velocity of blood 0.11 m/s. For 1.44 m/s, a vortex forms towards the inner wall. This vortex expands in size as the blood velocity increases. Finally, near the top and bottom surfaces of the artery with the maximum velocity of 0.1 m/s, some large vortexes are formed.

The second row shows the contour plots of the pressure profile for a healthy and stenosed artery at the proximal location, Figure 13:13. At the input port, parabolic-shaped pressure lines can be detected, and they appear to be practically parallel to the vertical line on the other side. Since proximal location is near the inlet, the pressure distribution is at its highest at the healthy artery. The pressure amplitude of the stenosed region is less than the healthy artery. Reduced pressures are recorded through the artery in all cases, but very low pressures are obtained following the stenosed area, indicating lower velocity at that location.

In Figure, the encapsulations show velocity and pressure, at a mid-distance stenosis where the artery is curved. At this location the results reveal lower values of velocity and pressure amplitude than the previous case. The first row shows the contour plots of the velocity profile for a healthy and stenosed artery at the mid location with same area. Higher velocity is observed in the core portion of the artery, whereas lower velocity is found at the wall. In the right side, the velocity contours of stenosed artery are shown. The velocity at peak flow for the middle stenosis is 2.79 m/s which is almost 80% lower than the proximal stenosis. Even though the stenosis severity is higher in the mid distance, the velocity is lower in this case. This indicates that, velocity parameter depends on the location more than the stenosis severity.

The second row shows the contour plots of the pressure profile for a healthy and stenosed artery at the mid location, Figure. Since mid-location is 2mm far from the proximal distance, the pressure distribution is lesser at the healthy artery. The pressure drop at the stenosed region is also less than in the previous case.

Case 1: Location- Proximal (without PDA) (Figure 13)

Case 2: Location- Mid (without PDA) (Figure 14)

In Figure 15, the encapsulations show lower velocity and pressure amplitude at stenosis than the hemodynamic parameters than the previous case for its location and the severity of the stenosis.

The first row shows the contour plots of the velocity profile for a healthy and stenosed artery at the mid location with same area. Because there is no slip, higher velocity is observed in the core portion of the artery, whereas lower velocity is found at the wall. In the right side, the velocity contours of stenosed artery are shown. The velocity at peak flow for the middle stenosis is 2.79 m/s which is almost 80% lower than the proximal stenosis. Even though the stenosis severity is higher in the mid distance, the velocity is lower here. This indicates that, velocity parameter depends on the location more than the stenosis severity.

The second row shows the contour plots of the pressure profile for a healthy and stenosed artery at the mid location. Since mid-location is 2mm far from the proximal distance, the pressure distribution is lesser at the healthy artery. The pressure drop at the stenosed region is also less than the previous case.

Case 3: Location- Distal (without PDA) (Figure 15)

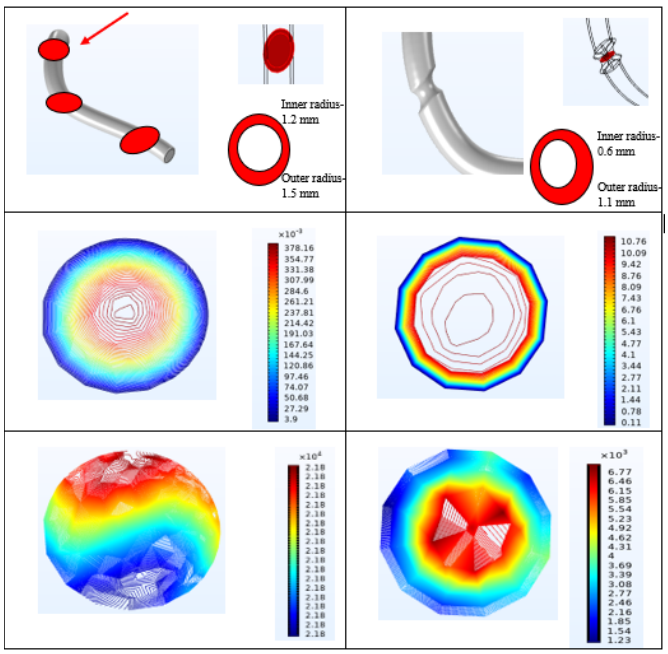

Figure 13: Velocity and pressure, with and without stenosis (healthy and 1-stenosis model).

In the RCA model (without PDA), the velocity varies from 378.16×10^{-3} m/s (healthy) to 10.76 m/s (1st stenosis) in the proximal location, from 373.02×10^{-3} m/s (healthy) to 2.79 m/s (2nd stenosis) in the mid location and from 381.96×10^{-3} m/s (healthy) to 2.47 m/s (3rd stenosis) in the distal location. This observation indicates that, the velocity profile is varying the most in the mid position where exists a bending curve.

The pressure varies from 2.18×10^{4} Pa (healthy) to 6.77×10^{4} Pa (1st stenosis) in the proximal location, from 2.17×10^{4} m/s (healthy) to 2.1×10^{4} Pa (2nd stenosis) in the mid location and from 2.17×10^{4} m/s (healthy) to 1.88×10^{4} Pa (3rd stenosis) in the distal location. This observation indicates that, the pressure profile is varying the most in the distal position as the fluid flows from the higher-pressure value to lower.

In Figure 16, Figure 17:17 and Figure 18:18, we have shown the RCA model (with PDA), and the velocity and pressure is higher in the branch stenosis than other locations. The first row in Figure 16 shows the contour plots of the velocity profile for a healthy and stenosed artery at the proximal location with same area. It shows the same variation as case 1 but its overall velocity at peak systole in the stenosed region is lower (2.78 m/s) than case 1. This shows the effect of the side branch PDA.

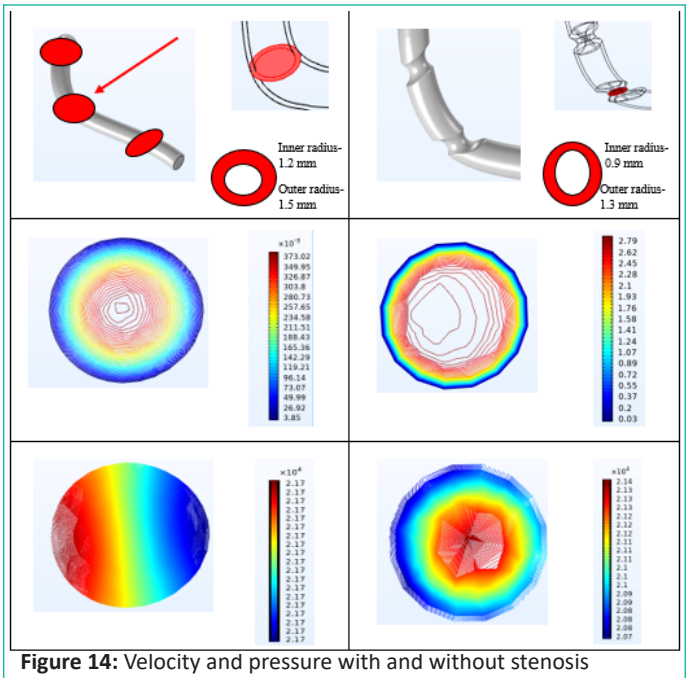

Figure 14: Velocity and pressure with and without stenosis (healthy and 2-stenosis model).

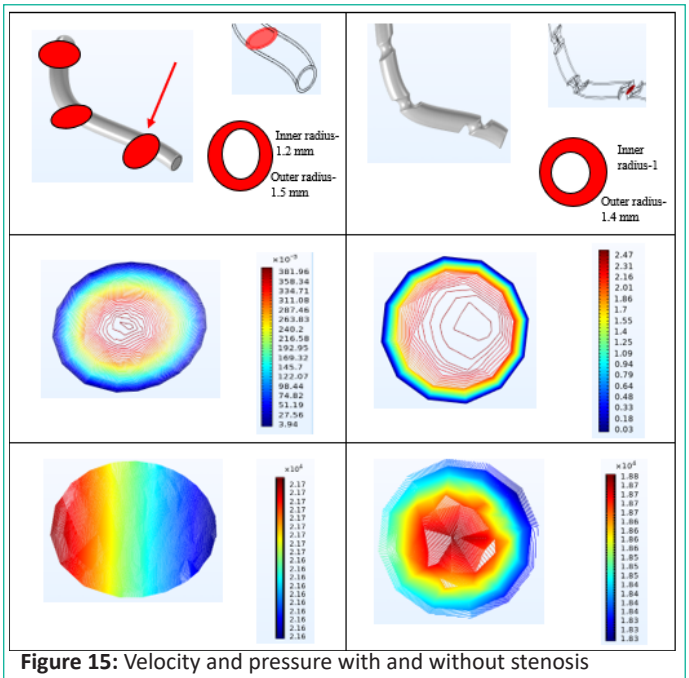

Figure 15: Velocity and pressure with and without stenosis (healthy and 3-stenosis model).

The second row shows the contour plots of the pressure profile for a healthy and stenosed artery at the proximal location. Since proximal location is near the inlet, the pressure distribution is at its highest at the healthy artery. The pressure amplitude of the stenosed region is less than the healthy artery. Reduced pressures are recorded through the artery in all cases, but very low pressures are obtained following the stenosed area, indicating lower velocity at that location. The pressure drop (2.26×10^{4} Pa) is higher than case 1 (6.67×10^{4} Pa) at the systolic case. This difference demonstrates the effect of the stenosis of PDA.

The first row in Figure 17:6 shows the contour plots of the velocity profile for a healthy and stenosed artery at the side branch with same area. It shows the same variation as case 2 but its overall velocity at peak systole in the stenosed region is lower (1.48 m/s) than case 2. This shows the effect of the side branch PDA.

The second row shows the contour plots of the pressure profile for a healthy and stenosed artery at the side branch. Since PDA is at distal location, the pressure distribution is at its lowest at the healthy artery. The pressure amplitude of the stenosed region is less than the healthy artery. Reduced pressures are recorded through the artery in all cases, but very low pressures are obtained following the stenosed area, indicating lower velocity at that location. The pressure drop (2.15×10^{4} Pa) is higher than case 2 (2.14×10^{4} Pa) at the systolic case. This difference demonstrates the effect of the stenosis of PDA.

The first row in Figure 18:17 shows the contour plots of the velocity profile for a healthy and stenosed artery at the distal location with same area. It shows the same variation as case 3 but its overall velocity at peak systole in the stenosed region is lower (1.49 m/s) than case 3. Since, case 3 and case 6 both shows the values for the distal location, this variation of the effect occurs for the side branch PDA.

Case 4: Location- Proximal (with PDA) (Figure 16)

Case 5: Location- Branch (with PDA) (Figure 17)

Case 6: Location- Distal (with PDA) (Figure 18)

The second row in Figure 18:18 shows the contour plots of the pressure profile for a healthy and stenosed artery at the distal location. So, the pressure distribution is at its lowest at the healthy artery. The pressure amplitude of the stenosed region is less than the healthy artery. Reduced pressures are recorded through the artery in all cases, but very low pressures are obtained following the stenosed area, indicating lower velocity at that location. The pressure drop (2.15×10^{4} Pa) is lower than case 3 (1.88×10^{4} Pa) at the systolic case. This difference demonstrates the effect of the stenosis of PDA.

In the RCA model (with PDA), The velocity varies from 500.3 × 10^{-3} m/s (healthy) to 2.78 m/s (1st stenosis) in the proximal location, from 298.63 × 10^{-3} m/s (healthy) to 1.49 m/s (2nd stenosis) in the PDA and from 298.63 × 10−3 m/s (healthy) to 1.49 m/s (3rd stenosis) in the distal location. This observation indicates that, the velocity profile is varying the most in the proximal position because the other two stenosis are in distal location. The pressure varies from 2.19 × 104 Pa (healthy) to 2.26 × 104 Pa (1st stenosis) in the proximal location, from 2.15 ×

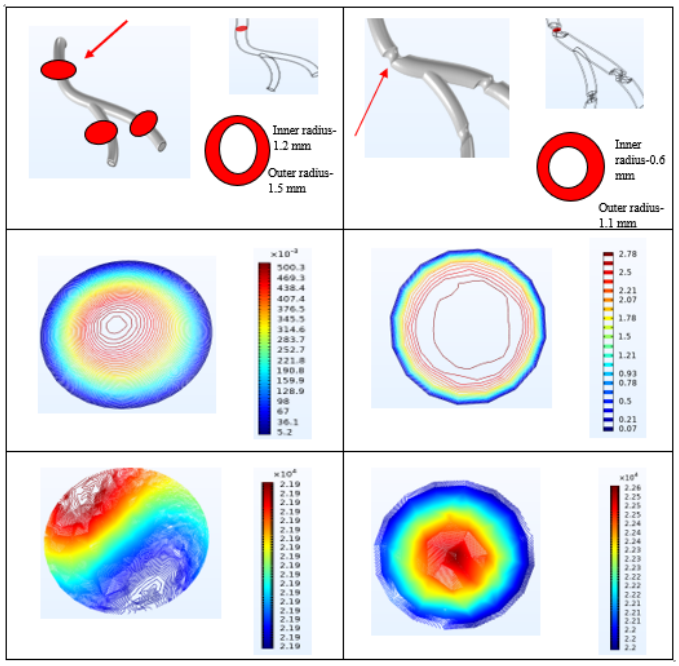

Figure 16: Cross-sectional area with and without stenosis (healthy and multiple stenosis model with PDA at proximal regime).

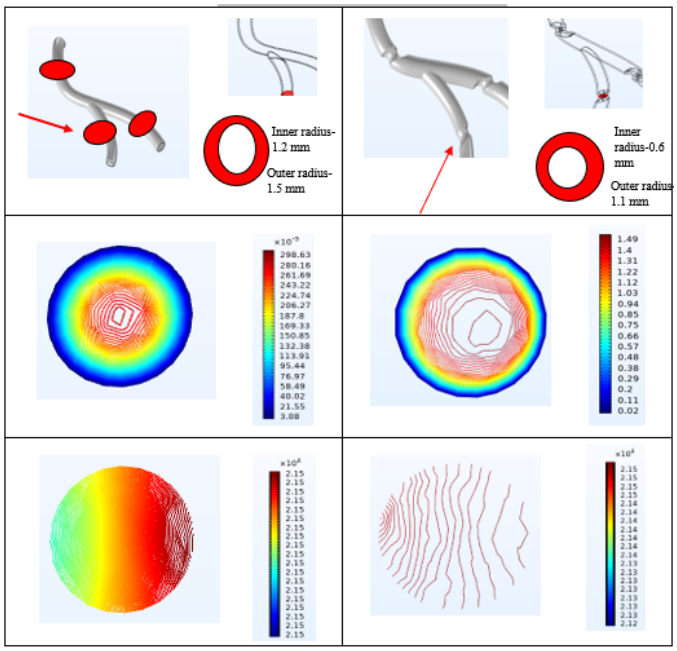

Figure 17: Cross-sectional area with and without stenosis (healthy and multiple stenosis model with PDA at branch regime).

104 m/s (healthy) to 2.00 × 104 Pa (2nd stenosis) in the PDA and from 2.15 × 104 m/s (healthy) to 2.15 × 104 Pa (3rd stenosis) i.e., uniform distribution in the distal location. This observation indicates that, the pressure profile is varying the most in the proximal position as the fluid flows from the higher-pressure value to lower. It's also varying in the other two location but the values are almost similar. This whole analysis indicates, that proximal location is the most crucial position for having a stenosis and the side branch PDA has a significant effect on the variation of the hemodynamic parameters. So, it is clear that, the hemodynamic parameters vary due to the location of the cross-sectional area and the geometry of the main body and the side branch. It can hence be concluded that the curvature and angulation have a significant effect on the hemodynamics analysis of RCAs and its correlation with atherosclerotic lesions.

In addition to these atherosclerotic variables, the development of stress in the arterial wall has a direct impact on the flow field pressure. Low pressure gradient is closely connected with

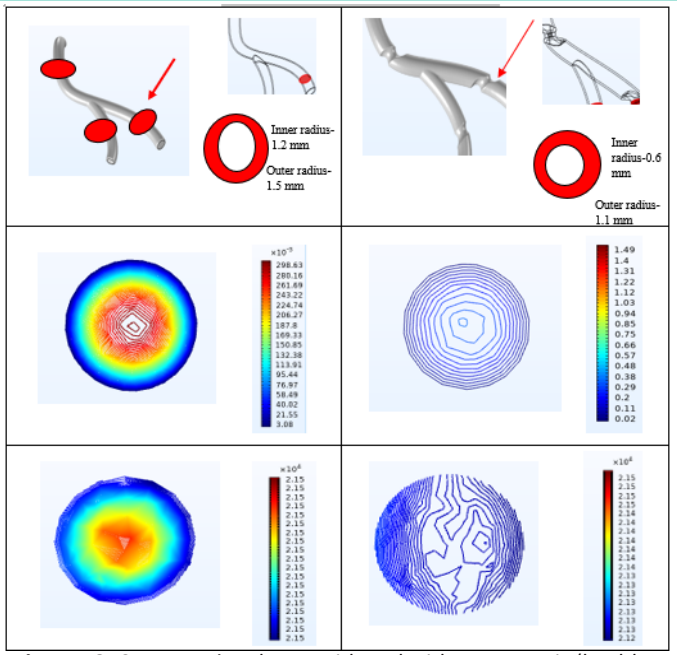

Figure 18: Cross-sectional area with and without stenosis (healthy and multiple stenosis model with PDA at distal regime).

atherosclerosis, according to studies on wall pressure and associated atherosclerosis [70]. Low- and high-pressure gradient are found in the same places as low and high WS at high curvature and branch points, suggesting that low- and high-pressure gradient might be another "Evaluation Index" for predicting plaque prone spots.

Hemodynamic Pattern due to the Position of Stenosis

In this section, we discuss the dependency of hemodynamics parameter (velocity, pressure) on arclength. The comparison shows that the velocity in healthy RCA is lower than the diseased RCA with respect to position which is indicated by arc length. We report the velocity profile along a one-dimensional line in the healthy artery at the position where the stenoses occurred [71]. The following graphs demonstrate the velocity distribution of the RCA model (with and without PDA). In Figure 19 it can be shown that the curvature has a significant effect on the velocity hemodynamics analysis of RCAs and its correlation with atherosclerotic lesions. The red one indicates the velocity amplitude for healthy model which is uniformly periodic. The other three graphs show the velocity amplitude of the various stenosis models. The green one varies the most as it is on the proximal part of the RCA.

In Figure 20, we have plotted the velocity amplitude for healthy and stenosed model of the branched RCA. The branched geometry varies even more than the bending geometry of the unbranched RCA. It can hence be concluded that not only the curvature has a significant effect on the pressure analysis of RCAs but also the branched geometry has an effect on it.

The pressure amplitude shows a huge difference as the its gradient depends on location more severely than any other hemodynamic parameter [65]. Pressure drop (from inlet to outlet) is significantly increased as the geometric complexity of the idealized models increased.

The following graphs for both models demonstrate that. The first graph (Figure 21) shows the comparison between healthy and multiple stenosis RCA model (without PDA) and the second graph (Figure 22) shows the comparison between healthy and multiple stenosis RCA model (with PDA).

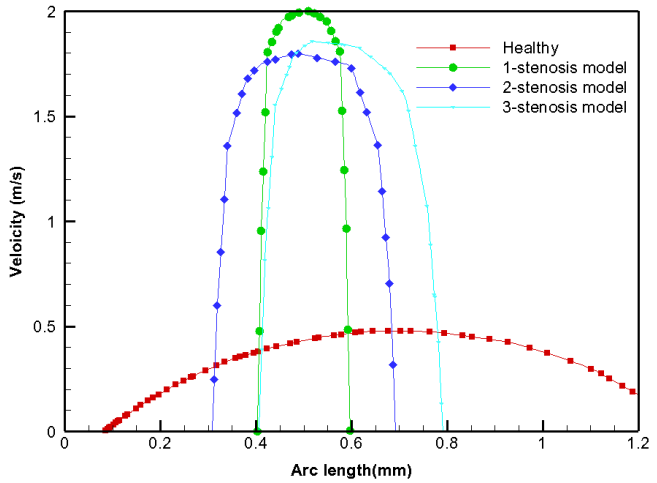

Figure 19: Velocity profile vs position due to multiple stenosis (without PDA).

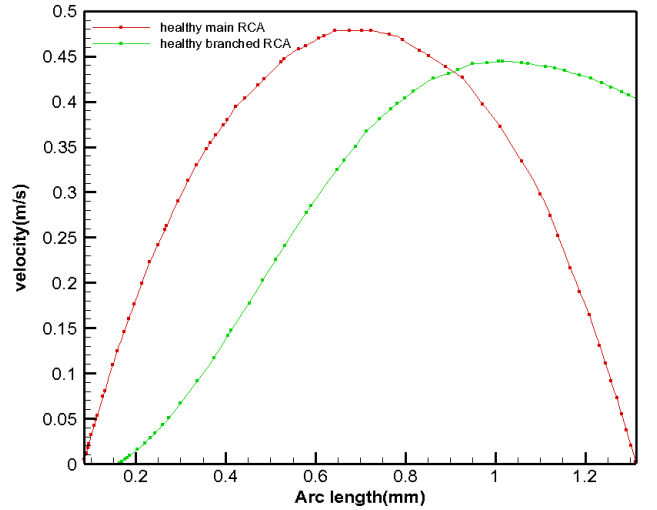

Figure 20: Velocity profile vs position due to multiple stenosis (with PDA)

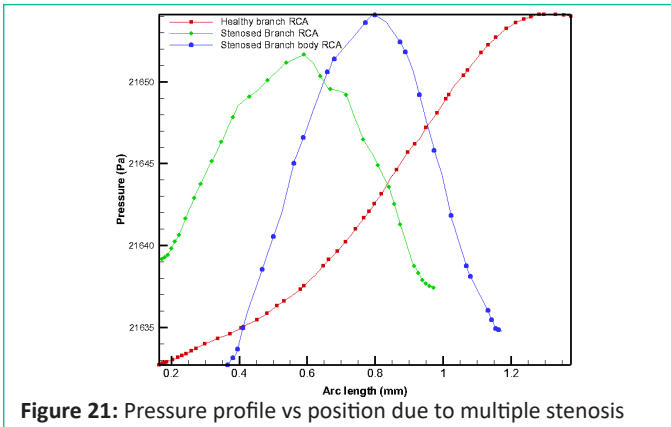

Figure 21: Pressure profile vs position due to multiple stenosis (without PDA).

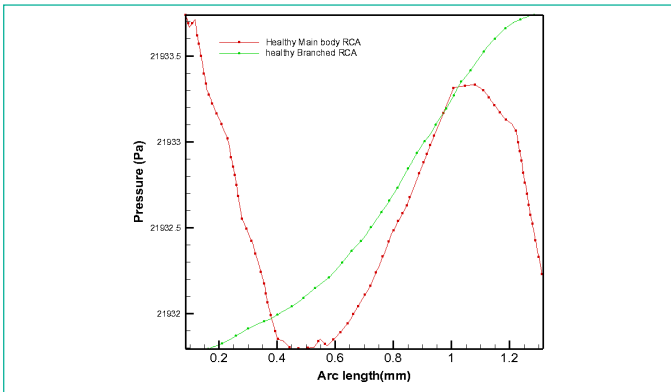

Figure 22: Pressure profile vs position due to multiple stenosis (with PDA).

From Figure 21, it can hence be concluded that the geometry of curvature has a significant effect on the pressure hemodynamics analysis of RCAs and its correlation with atherosclerotic lesions. The red one indicates the pressure amplitude for healthy model which is uniformly periodic. The other three graphs show the pressure amplitude of the various stenosis models. The blue one varies the most as it is on the bending mid part of the RCA

In Figure 22, we have plotted the pressure amplitude for healthy and stenosed model of the branched RCA. The branched geometry varies even more than the bending geometry of the unbranched RCA. It can hence be concluded that not only the curvature has a significant effect on the pressure hemodynamics analysis of RCAs but also the branched geometry.

The low and/or oscillatory wall shear stress-induced inflammatory activation of the endothelium typically occurs at the inner bend of curved arteries and branches. Plaque rupture is responsible for two-thirds of acute coronary syndromes. The event appears to be induced by endothelial erosion in one-third of the cases, which shows a thrombus underlying a non-ruptured plaque [66]. The processes that control plaque erosion are less well understood than those that control plaque rupture. It has been claimed that erosion can be caused by both high and low wall shear stress. However, because wall shear stress as it is now measured lacks adequate sensitivity and specificity to reliably forecast clinically significant growth of atherosclerotic plaques, more methodological advancements will be required. *In vitro* and *in vivo* animal studies demonstrate that wall shear stress is a potent modulator of endothelial function and influences the development of atherosclerosis. As such, the major clinical interest in wall shear stress arises from its ability to identify patients at risk for future cardiovascular events or complications after stent placement. Low wall shear stress has been linked to non-culprit MACE and future angiographically induced revascularization. Future myocardial infarctions have been linked to high wall shear stress. In this study we analyze the Wall Stress (WS) induced by the blood flow. This result is more significant compared to the WSS because it provides more information about the stresses acting on the wall near the plaque location.

Conclusions

This work provides a framework for developing a parametric study that is built on idealized coronary models, which we have used to evaluate the effect of curvature of RCAs, side branch PDA and various location of the stenosis on the hemodynamic characteristics. We predicted the physiological Response of one of the main Coronary Arteries (RCA) flow conditions by using a noninvasive approach. We have employed appropriate BCs in the inlet and outlet with a three-element WK model. The pulsatile boundary profiles produced physiological behaviors in the healthy, single stenosis and multiple stenosis models. In the diseased RCA models, the proximal moderate and distal severe stenoses produced higher WS in the RCA (without PDA). In RCA with PDA, the WS is much higher in proximal moderate stenosis than distal severe stenosis in both main segment and PDA branch. The velocity and pressure values are higher in the proximal moderate stenosis than the distal severe stenosis. We have visualized the cross-sectional area demonstrating the hemodynamic parameters and also the line graphs of the parameters for approximating the location of stenosis more precisely.

These findings can help understand the following facts:

➢ This study shows that proximal stenosis is more detrimental than distal stenosis, might lead to a better understanding of how hemodynamic features affect coronary artery disease measures.

➢ This knowledge might help researchers improve physiological evaluation of defective RCA models [72]. The findings indicate coronary hemodynamic parameters that clinicians may utilize to diagnose coronary problems using a visualization approach.

➢ It has been shown that the local velocity streamline and pressure drop regions sited at the plaques prone points are consistent with the data derived from literature, and show a marked difference in both magnitude and spatial distribution of velocity and pressure in all the simulated models, thereby demonstrating the hemodynamics differences among the models with diversity in their anatomy.

➢ This approach might be used to predict the severity of coronary artery disease since it is noninvasive, low-risk, and low-cost.

➢ This CFD research of coronary hemodynamic parameter field analyzed for each stenosis artery stenosis has revealed that RCA geometry has a significant influence on flow pattern and hemodynamic parameters including velocity, pressure, and WS.

➢ This is significant since it has previously been observed that changes in the intracoronary flow pattern around the coronary plaque can be a risk factor for plaque rupture [73] and thrombotic consequences, as well as that new stenosis can develop when the lumen narrows. As a result, in order to enhance the diagnosis of hazardous and substantial stenosis, a geometrical parameter should be examined and taken into account in clinical practice.

We expect that the data can be used in therapeutic settings; nevertheless, there are several limits to this process that will require additional research.

Limitations

Although the study suggests a correlation between various RCA attributes and favorable hemodynamic circumstances that promote atherosclerotic plaque development, there are several drawbacks. Due to the substantial roughness resulting from the import procedure, the models are built on an open program "Free CAD", necessitating vessel smoothing. For the simulations, we have used a commercial software for the time independent problems which took substantial time due to machine limitations.

A consistent artery wall thickness was imposed, which might lead to over dimensioning in main segments and side branches, increasing their rigidity. Furthermore, the 5-parameters Mooney–Rivlin constitutive model [74] for coronary arteries could be used in the future to describe the artery wall as a nonlinear hyper elastic material, which was widely employed by other researchers. Other constitutive models, however, might be used to modify the outcomes. Furthermore, the expansion and contraction of the heart, which might impact coronary artery flow [75], were not taken into consideration.

Inertia can play a crucial role in coronary blood flow, causing more asymmetry in the velocity profiles and therefore in the WS, due to the enormous motion of the ventricles. These constraints, however, are regarded appropriate for the statistical analysis [76] because they apply to all patient-specific situations and all the required realistic techniques go beyond what is accessible in the literature.

References

1. Baum SJ, Kris-Etherton PM, Willett WC, Lichtenstein AH, Rudel LL, Maki KC, et al. Fatty acids in cardiovascular health and disease: A comprehensive update. J Clin Lipidol. 2012; 6: 216-234.
2. Bonilla HMG, Ganta N, Awan AA, Asare IO, "Abstract 15360. Coronary artery dominance, anatomical variants and anomalies in African American population. Circulation. 2020; 142: A15360-A15360.
3. Wong KKL, Wu J, Liu G, Huang W, Ghista DN. Coronary arteries hemodynamics: effect of arterial geometry on hemodynamic parameters causing atherosclerosis. Med Biol Eng Comput. 2020; 58: 1831-1843.
4. Duchoud L, Sandre-Mouly C, Sandu K. Congenital tracheal stenosis: from clinic to treatment. Rev Med Suisse. 2019; 15: 1765-1768.
5. Ferdows M, Hoque KE, Bangalee MZ, Xenos MA. Engineering Wall shear stress indicators influence the regular hemodynamic conditions in coronary main arterial diseases: cardiovascular abnormalities. Comput Methods Biomech Biomed Engin. 2022; 25: 1-14.
6. Culak J, Peet YV, Chopp DL. Smooth Mesh Generation for Numerical Analysis of Blood Vessel Fluid Flow. ASME. 2011; 927-928.
7. Mynard JP, Smolich JJ. Influence of anatomical dominance and hypertension on coronary conduit arterial and microcirculatory flow patterns: A multiscale modeling study. Am J Physiol - Hear Circ Physiol. 2016; 311: 11-23.
8. Watanabe Y. Determinants of In-Hospital Death in Acute Myocardial Infarction With Triple Vessel Disease. Int Heart J. 2016; 57: 697-704.
9. Sanaani A, Yandrapalli S, Jolly G, Paudel R, Cooper HA, Aronow WS. Correlation between electrocardiographic changes and coronary findings in patients with acute myocardial infarction and single-vessel disease. Ann Transl Med. 2017; 5: 347.
10. Hoque KE, Sawall S, Hoque MA, Hossain MS. Hemodynamic Simulations to Identify Irregularities in Coronary Artery Models. J Adv Math Comput Sci. 2018; 28: 1-19.
11. Dan K, Shinoda A, Tsuzura D, Garcia-Garcia HM. Triple coronary vessel disease including double vessel chronic total occlusion: Quantitative flow ratio minimizes injury of the single vessel that provides collaterals. Cardiology journal. 2019; 26: 407-409.
12. Peng L, Guo X, Gao Y, Guo Q, Zhang J, et al.. Impact of right coronary dominance on triple-vessel coronary artery disease: A cross-sectional study. Medicine (Baltimore. 2018; 97: e11685.
13. Parikh NI, Honeycutt EF, Roe MT, Neely M, Rosenthal EJ, et al. Left and Codominant Coronary Artery Circulations Are Associated With Higher In-Hospital Mortality Among Patients Undergoing Percutaneous Coronary Intervention for Acute Coronary Syndromes. Circ Cardiovasc Qual Outcomes. 2012; 5: 775-782.
14. Wang L. Association between coronary dominance and acute inferior myocardial infarction: a matched, case-control study. BMC Cardiovasc Disord. 2019; 19: 35.
15. Kafi O, Khatib NE, Tiago J, Sequeira A. Numerical simulations of a 3D fluid-structure interaction model for blood flow in an atherosclerotic artery. Math Biosci Eng. 2017; 14: 179-193.

16. Pinho N, Sousa LC, Castro CF, Antonio CC, Carvalho M, et al. The Impact of the Right Coronary Artery Geometric Parameters on Hemodynamic Performance. Cardiovasc Eng Technol. 2019; 10: 257-270.

17. Gibson CM, Diaz L, Kandarpa K, Sacks FM, Pasternak RC, et al. Relation of vessel wall shear stress to atherosclerosis progression in human coronary arteries. Arterioscler Thromb a J Vasc Biol. 1993; 13: 310-315.

18. Pedersen EM, Oyre S, Agerbaek M, Kristensen IB, Ringgard S, et al. Distribution of early atherosclerotic lesions in the human abdominal aorta correlates with wall shear stresses measured in vivo. Eur J Vasc Endovasc Surg. 1999; 18: 328-333.

19. Wang Q. MRI-based patient-specific human carotid atherosclerotic vessel material property variations in patients, vessel location and long-term follow up. PLoS One. 2017; 12: 0180829.

20. Failer L, Minakowski P, Richter T. On the Impact of Fluid Structure Interaction in Blood Flow Simulations. Vietnam J Math. 2021; 49: 169-187.

21. Park JB. Computational fluid dynamic measures of wall shear stress are related to coronary lesion characteristics. Heart. 2016; 102: 1655-1661.

22. Zhong L, Zhang JM, Su B, Tan RS, Allen JC, Kassab GS. Application of patient-specific computational fluid dynamics in coronary and intra-cardiac flow simulations: Challenges and opportunities. Front Physiol. 2018; 9.

23. Liu B, Tang D. Computer simulations of atherosclerotic plaque growth in coronary arteries. Mol Cell Biomech. 2010; 7: 193-202.

24. Johnston BM, Johnston PR, Corney S, Kilpatrick D. Non-Newtonian blood flow in human right coronary arteries: transient simulations. J Biomech. 2006; 39: 1116-1128.

25. Liu H. Consistency in Geometry Among Coronary Atherosclerotic Plaques Extracted From Computed Tomography Angiography. Front Physiol. 2021; 12.

26. Rinehart S, Vazquez G, Qian Z, Murrieta L, Christian K, Voros S. Quantitative measurements of coronary arterial stenosis, plaque geometry, and composition are highly reproducible with a standardized coronary arterial computed tomographic approach in high-quality CT datasets. J Cardiovasc Comput Tomogr. 2011; 5: 35-43.

27. Liu H. Extraction of Coronary Atherosclerotic Plaques From Computed Tomography Imaging: A Review of Recent Methods. Front Cardiovasc Med. 2021; 8: 597568.

28. Caruso MV, Rosa S, Indolfi C, Fragomeni G. Computational analysis of stenosis geometry effects on right coronary hemodynamics. In: 2015 37th Annual International Conference of the IEEE Engineering in Medicine and Biology Society (EMBC. 2015; 981-984.

29. Vasques MT, Mori M, Laganá DC. Three-dimensional printing of occlusal devices for temporomandibular disorders by using a free CAD software program: A technical report. J Prosthet Dent. 2020; 123: 232-235.

30. Kaufmann P, Vassalli G, Lupi-Wagner S, Jenni R, Hess OM. Coronary artery dimensions in primary and secondary left ventricular hypertrophy. J Am Coll Cardiol. 1996; 28: 745-750.

31. Kamman AV. Predictors of Stable Aortic Dimensions in Medically Managed Acute Aortic Syndromes. Ann Vasc Surg. 2017; 42: 143-149.

32. H. KE, Zaman EETN, Ferdows M, Xenos MA. Effect of Angle Bifurcation and Stenosis in Coronary Arteries: An Idealized Model Study. BioMed Res J. 2020; 4: 214-228.

33. Manchester EL, Pirola S, Salmasi MY, O'Regan DP, Athanasiou T, Xu XY. Evaluation of Computational Methodologies for Accurate Prediction of Wall Shear Stress and Turbulence Parameters in a Patient-Specific Aorta. Front Bioeng Biotechnol. 2022; 10: 836611.

34. Xenos M. Patient-based abdominal aortic aneurysm rupture risk prediction with fluid structure interaction modeling. Ann Biomed Eng. 2010; 38: 3323-3337.

35. Chaichana T, Sun Z, Jewkes J. Hemodynamic impacts of left coronary stenosis: A patient-specific analysis. Acta Bioeng Biomech. 2013; 15: 107-112.

36. Balzani D. Numerical modeling of fluid–structure interaction in arteries with anisotropic polyconvex hyperelastic and anisotropic viscoelastic material models at finite strains. Int j numer method biomed eng. 2016; 32: 02756.

37. Xenos MA. An Euler–Lagrange approach for studying blood flow in an aneurysmal geometry. Proc R Soc A Math Phys Eng Sci. 2017; 473: 20160774,.

38. Torii R. Fluid–structure interaction analysis of a patient-specific right coronary artery with physiological velocity and pressure waveforms. Commun Numer Methods Eng. 2009; 25: 565-580.

39. Averweg S, Schwarz A, Nisters C, Schröder J. A least-squares finite element approach to model fluid-structure interaction problems. PAMM. 2019; 19: 201900204.

40. Robertson AM, Sequeira A, Owens RG. Rheological models for blood. In: Formaggia L, Quarteroni A, Veneziani A, editors. Cardiovascular Mathematics: Modeling and simulation of the circulatory system. Milano: Springer Milan. 2009; 211–41.

41. Rambhia SH. Microcalcifications increase coronary vulnerable plaque rupture potential: a patient-based micro-CT fluid-structure interaction study. Ann Biomed Eng. 2012; 40: 1443-1454.

42. Jahangiri M, Saghafian M, Sadeghi MR. Numerical simulation of non-Newtonian models effect on hemodynamic factors of pulsatile blood flow in elastic stenosed artery. J Mech Sci Technol. 2017; 31: 1003-1013.

43. Chakravarty S, Mandal PK. Two-dimensional blood flow through tapered arteries under stenotic conditions. Int J Non Linear Mech. 2000; 35: 779-793.

44. Moon JY, Suh DC, Lee YS, Kim YW, Lee JS. Considerations of blood properties, outlet boundary conditions and energy loss approaches in computational fluid dynamics modeling. Neurointervention. 2014; 9: 1-8.

45. Hoque KE, Ferdows M, Sawall S, Tzirtzilakis EE. The effect of hemodynamic parameters in patient-based coronary artery models with serial stenoses: normal and hypertension cases. Comput Methods Biomech Biomed Engin. 2020; 23: 467-475.

46. Yeasmin S, Billah MM, Molla MZ, Hoque KE. Numerical analysis of unsteady mixed convection heat transfer characteristics of nanofluids confined within a porous lid-driven L-shaped cavity. Int J Thermofluids. 2022; 16: 100218.

47. Aboelkassem Y, Virag Z. A hybrid Windkessel-Womersley model for blood flow in arteries. J Theor Biol. 2019; 462: 499-513.

48. Madhavan S, Kemmerling EMC. The effect of inlet and outlet boundary conditions in image-based CFD modeling of aortic flow. Biomed Eng Online. 2018; 17: 66.

49. Pirola S, Cheng Z, Jarral OA, O'Regan, Pepper JR, et al. On the choice of outlet boundary conditions for patient-specific analysis of aortic flow using computational fluid dynamics. J Biomech. 2017; 60: 15-21.

50. Westerhof N, Lankhaar J-W, Westerhof BE. The arterial Windkessel. Med Biol Eng Comput. 2009; 47: 131-141.

51. Liang X. Biomechanical factors in coronary vulnerable plaque risk of rupture: intravascular ultrasound-based patient-specific fluid-structure interaction studies. Coron Artery Dis. 2013; 24: 75-87.

52. Nammakie E, Niroomand-Oscuii H, Koochaki M, Ghalichi F. Computational fluid dynamics-based study of possibility of generating pulsatile blood flow via a continuous-flow VAD. Med Biol Eng Comput. 2017; 55: 167-178,.

53. Pandey R, Kumar M, Srivastav VK. Numerical computation of blood hemodynamic through constricted human left coronary artery: Pulsatile simulations. Comput Methods Programs Biomed. 2020; 197: 105661,.

54. Kokalari I, Karaja T, Guerrisi M. Review on lumped parameter method for modeling the blood flow in systemic arteries. J Biomed Sci Eng. 2013; 06: 92-99.

55. Zhang S, Luo X, Cai Z. Three-dimensional flows in a hyperelastic vessel under external pressure. Biomech Model Mechanobiol. 2018; 17: 1187-1207.

56. Calamante F. Arterial input function in perfusion MRI: a comprehensive review. Prog Nucl Magn Reson Spectrosc. 2013; 74: 1-32.

57. Armour CH. The influence of inlet velocity profile on predicted flow in type B aortic dissection. Biomech Model Mechanobiol. 2021; 20: 481-490.

58. Bit A. Three dimensional numerical analysis of hemodynamic of stenosed artery considering realistic outlet boundary conditions. Comput Methods Programs Biomed. 2020; 185: 105163.

59. Hoque KE, Ferdows M, Sawall S, Tzirtzilakis EE, Xenos MA. The impact of hemodynamic factors in a coronary main artery to detect the atherosclerotic severity: Single and multiple sequential stenosis cases. Phys Fluids. 2021; 33.

60. Yang Y, Jäger W, Neuss-Radu M, Richter T. Mathematical modeling and simulation of the evolution of plaques in blood vessels. J Math Biol. 2016; 72: 973-996.

61. Richter T. A monolithic geometric multigrid solver for fluid-structure interactions in ALE formulation. Int J Numer Methods Eng. 2015; 104: 372-390.

62. Ha ST, Ngo LC, Saeed M, Jeon BJ, Choi H. A comparative study between partitioned and monolithic methods for the problems with 3D fluid-structure interaction of blood vessels. J Mech Sci Technol. 2017; 31: 281-287.

63. Failer L, Richter T. A Parallel Newton Multigrid Framework for Monolithic Fluid-Structure Interactions. J Sci Comput. 2020; 82: 1-27.

64. Kenny A, Wisbey CR, Shapiro LM. Profiles of coronary blood flow velocity in patients with aortic stenosis and the effect of valve replacement: a transthoracic echocardiographic study. Heart. 1994; 71: 57-62.

65. Lipscomb K, Hooten S. Effect of stenotic dimensions and blood flow on the hemodynamic significance of model coronary arterial stenoses. Am J Cardiol. 1978; 42: 781-792.

66. Hoque KE, Ali MH. The Impact of Hemodynamic Parameters in 3d Idealized Coronary Artery Normal and Disease Models. Adv Mech Eng Technol. 2022; 5: 1-15.

67. Faccenda F, Usui Y, Spencer MP. Doppler measurement of the pressure drop caused by arterial stenosis: an experimental study: a case report. Angiology. 1985; 36: 899-905.

68. Buradi A, Mahalingam A. Effect of stenosis severity on wall shear stress based hemodynamic descriptors using multiphase mixture theory. J Appl Fluid Mech. 2018; 11: 1497-1509.

69. Hoque KE, Ferdows M, Sawall S, Tzirtzilakis EE, Xenos MA. Hemodynamic characteristics expose the atherosclerotic severity in coronary main arteries: One-dimensional and three-dimensional approaches. Phys Fluids. 2021; 33: 121907.

70. Giannoglou GD, Soulis JV, Farmakis TM, Giannakoulas GA, Parcharidis GE, et al. Wall pressure gradient in normal left coronary artery tree. Med Eng Phys. 2005; 27: 455-464.

71. Liu G, Wu J, Ghista DN, Huang W, Wong KKL. Hemodynamic characterization of transient blood flow in right coronary arteries with varying curvature and side-branch bifurcation angles. Comput Biol Med. 2015; 64: 117-126.

72. Sousa L, Castro C, António C, Chaves RUI. Computational Techniques and Validation of Blood Flow Simulation. 2011; 8: 145-155.

73. Bentzon JF, Otsuka F, Virmani R, Falk E. Mechanisms of plaque formation and rupture. Circ Res. 2014; 114: 1852-1866.

74. Karimi A, Navidbakhsh M, Shojaei A, Hassani K, Faghihi S. Study Of Plaque Vulnerability In Coronary Artery Using Mooney–Rivlin Model: A Combination Of Finite Element And Experimental Method. Biomed Eng Appl Basis Commun. 2014; 26: 1450013.

75. Fan L, Yao J, Yang C, Xu D, Tang D. Modeling Active Contraction and Relaxation of Left Ventricle Using Different Zero-load Diastole and Systole Geometries for Better Material Parameter Estimation and Stress/Strain Calculations. Mol Cell Biomech. 2016; 13: 33-55.

76. Knight J. Choosing the optimal wall shear parameter for the prediction of plaque location-A patient-specific computational study in human right coronary arteries. Atherosclerosis. 2010; 211: 445-450.